https://doi.org/10.5194/acp-2019-534
Preprint. Discussion started: 23 July 2019

Atmospheric Chemistry and Physics Discussions

Reassessment of the common concept to derive the surface cloud radiative forcing in the Arctic: Consideration of surface albedo – cloud interactions

Johannes Stapf[1], André Ehrlich[1], Evelyn Jäkel[1], Christof Lüpkes[2], and Manfred Wendisch[1]

[1]Leipzig Institute for Meteorology (LIM), University of Leipzig, Germany
[2]Alfred Wegener Institute for Polar and Marine Research, Bremerhaven, Germany

Correspondence: Johannes Stapf (johannes.stapf@uni-leipzig.de)

Abstract. The concept of cloud radiative forcing (CRF) is commonly used to quantify the warming or cooling effect due to clouds on the radiative energy budget (REB). In the Arctic, radiative interactions between micro- and macrophysical properties of clouds and the surface influence the CRF and complicate its estimate obtained from observations or models. In this study the individual components and processes related to the surface CRF are analysed separately using simulations and measurement from low-level airborne observations of the REB in the heterogeneous springtime marginal sea ice zone (MIZ). The measurements were obtained during the Arctic CLoud Observations Using airborne measurements during polar Day (ACLOUD) campaign. The effect of changing surface albedo, due to the presence of clouds, and its dependence on cloud optical thickness was found to be relevant for the estimation of the solar CRF. A method to correct this albedo effect by retrieving the cloud-free surface albedo from observations under cloudy conditions is proposed. The application of this new concept to ACLOUD data shows, that the estimated average solar cooling effect by clouds almost doubles over snow and ice covered surfaces (-63 $\mathrm{W\,m^{-2}}$ instead of -33 $\mathrm{W\,m^{-2}}$), if surface albedo-cloud interactions are considered. Concerning the seasonal cycle of the surface albedo, this effect would potentially enhance solar cooling in periods where cold snow and ice dominate the surface and weaken the cooling by optical thin clouds and surface albedos commonly found during the summertime Arctic melting season. These findings suggest, that the surface albedo-cloud interaction needs to be represented in global climate models and in long-term observations to obtain a realistic estimate of the solar CRF and a reasonable representation of cloud radiative feedback mechanisms in the Arctic and to quantify the role of clouds in Arctic amplification.

1 Introduction

Interdisciplinary research conducted within the last decades has led to a broader, but not yet complete understanding of the rapid and, compared to mid-latitudes, enhanced warming in the Arctic (so-called Arctic amplification), which is triggered by global warming (Gillett et al., 2008; Overland et al., 2011; Serreze and Barry, 2011; Stroeve et al., 2012; Jeffries et al., 2013; Cohen et al., 2014; Wendisch et al., 2017). Since the interrelationships of physical processes, responsible for the Arctic amplification are complex and difficult to observe, climate models are needed to quantify the individual contribution of potential feedback processes to Arctic climate change (Screens and Simmonds, 2010; Pithan and Mauritsen, 2014). However, the model

https://doi.org/10.5194/acp-2019-534
Preprint. Discussion started: 23 July 2019

Atmospheric Chemistry and Physics Discussions

results show a large spread in representing the feedback mechanisms. One prominent example is the cloud feedback, which includes the effects of an increasing cloud amount in the Arctic. While the cooling cloud radiative effect (reflection of solar radiation back to space causing a near-surface cooling of the Arctic surface) dominates in summer, a warming cloud radiative effect enhances the near-surface air temperature in winter, when the emitted terrestrial radiation determines the surface energy budget. In order to enable reliable model projections of future climate changes in the Arctic, the understanding of the individual physical processes and feedback mechanisms of Arctic amplification is required (Pithan and Mauritsen, 2014; Goosse et al., 2018).

To quantify the instantaneous radiative effect of clouds on the surface radiative energy budget (REB), the cloud radiative forcing (CRF, expressed as ΔF) is defined as the difference between the net radiative energy flux densities,

$$F_{\mathrm{net}} = F^{\downarrow} - F^{\uparrow}, \tag{1}$$

also called irradiances, in cloudy (all-sky) ($F_{\mathrm{net,cld}}$) and cloud-free ($F_{\mathrm{net,cf}}$) conditions (Ramanathan et al., 1989),

$$\Delta F = F_{\mathrm{net,cld}} - F_{\mathrm{net,cf}}. \tag{2}$$

A warming effect of clouds at the surface will be induced if the net radiative flux densities in a cloudy atmosphere are larger than in corresponding cloud-free conditions. To derive the CRF from observations, simultaneous measurements of net irradiances in cloudy and cloud-free situations would be needed, which is impossible from a practical point of view. Therefore, the net irradiances of the cloud-free state are commonly obtained from radiative transfer simulations based on measurements of the observed surface conditions.

The downward terrestrial irradiance in cloud-free atmospheric conditions ($F^{\downarrow}_{\mathrm{t,cf}}$) depends on the profiles of atmospheric temperature, absorber gas and aerosol particle concentrations. In the solar wavelength range, $F^{\downarrow}_{\mathrm{s,cf}}$ is influenced by solar zenith angle (SZA), atmospheric profiles of gases and aerosol particle properties, as well as the surface albedo. To estimate the cloud-free atmospheric state, the input of the radiative transfer simulations is based on observations of the atmosphere and surface conditions in the cloudy state. However, e.g., the surface albedo in cloudy conditions is not necessarily identical to the one in a cloud-free atmosphere. In the Arctic, the surface albedo, determining the reflected solar radiation at the surface, depends on the snow and sea ice properties, such as specific surface area (SSA, equivalent to the snow grain size), surface roughness, snow height and density, the SZA, but also on the cloud optical thickness (Warren, 1982; Gardner and Sharp, 2010), which alters the spectral shape of the surface albedo and the angular distribution of the reflection.

In particular the spectral distribution of the incoming irradiance is shifted to shorter wavelengths in overcast conditions due to absorption within the clouds. In combination with the spectral shape of the snow albedo characterized by higher values for short wavelengths, this effect tends to increase the broadband albedo in cloudy conditions (Grenfell and Perovich, 2008). Furthermore, clouds induce a more isotropic illumination of the surface compared to cloud-free conditions where the direct solar radiation dominates the radiation field. In general, the snow albedo decreases with decreasing SZA (Warren, 1982). In the Arctic with prevailing high SZAs, clouds decrease the effective SZA to approximately 50° compared to cloud-free situation (Warren, 1982), and thus, have a diminishing effect on the surface albedo. Both processes have been parameterized, for

https://doi.org/10.5194/acp-2019-534
Preprint. Discussion started: 23 July 2019

Atmospheric Chemistry and Physics Discussions

example by Gardner and Sharp (2010) based on simulations, however, their impact on estimates of the CRF in the Arctic have not yet been evaluated.

In this study, the components of CRF, obtained by radiative transfer simulations, are investigated to improve the estimate of the total (solar plus terrestrial) CRF from observations and modelling in the Arctic environment. A method is described to retrieve the surface broadband albedo in a cloud-free atmosphere from measurements under cloudy conditions, and to account for the surface albedo heterogeneity, which induces uncertainties in the assumed cloud-free downward solar irradiance. An application of the approach to airborne low-level (below cloud) observations of REB in the marginal sea ice zone (MIZ) close to Svalbard during the Arctic CLoud Observations Using airborne measurements during polar Day (ACLOUD) campaign (Wendisch et al., 2019) is shown. This dataset extends available REB and CRF observations in the Arctic including horizontal variability in the heterogeneous MIZ.

2 Observation and modelling

2.1 Airborne measurements during ACLOUD

The cloudy atmospheric boundary layer (ABL) in the MIZ north west of Svalbard was studied with two aircraft during the ACLOUD campaign performed in spring between 23 May and 26 June 2017 (Wendisch et al., 2019). Part of the flights with the research aircraft Polar 5 and Polar 6 from the Alfred-Wegener Institute (AWI) were dedicated to characterize the near-surface radiative energy budget below ABL clouds. From all flights, 16 hours of data measured below an altitude of 250 m (average 80 m) covering a distance of 3700 km were investigated in this paper. The sea ice concentration observed along the low-level flight tracks by instruments mounted at the aircraft is displayed in Fig. 1, together with a (Moderate Resolution Imaging Spectroradiometer) MODIS satellite image illustrating a sea ice distribution being typical for end of May and June 2017. The red (80 %) and light-blue (15 %) contour lines indicate the average sea ice concentration during the ACLOUD campaign calculated from daily sea ice data (Spreen et al., 2008). During ACLOUD the location of the sea ice edge was almost stationary (Knudsen et al., 2018). In general, the sea ice was more compact (higher concentration) north of 81° N and rather heterogeneous towards the west and closer to the open ocean. The low-level flights of Polar 5 and 6 are almost equally distributed over these different sea ice conditions. The majority of flights (66 %) were over sea ice ($I_\mathrm{f} > 80\,\%$), leaving about 17 % over the MIZ as well as 17 % over open ocean ($I_\mathrm{f} < 15\,\%$). As the dataset is merged from different flights covering about six weeks of measurements, it comprises various sea ice characteristics and synoptic situations (Knudsen et al., 2018). However, the data set is still limited and should be considered as a snapshot of the late spring conditions in this region.

2.2 Instrumentation

The instrumentation of Polar 5 and Polar 6 during the ACLOUD campaign is described by Wendisch et al. (2019) as well as by Ehrlich et al. (2019b). The necessary processing of the Pyranometer and Pyrgeometer data (Stapf et al., 2019), which were used to derive the REB from ACLOUD observations, is described in Ehrlich et al. (2019b). Surface brightness temperature

https://doi.org/10.5194/acp-2019-534
Preprint. Discussion started: 23 July 2019

Atmospheric Chemistry and Physics Discussions

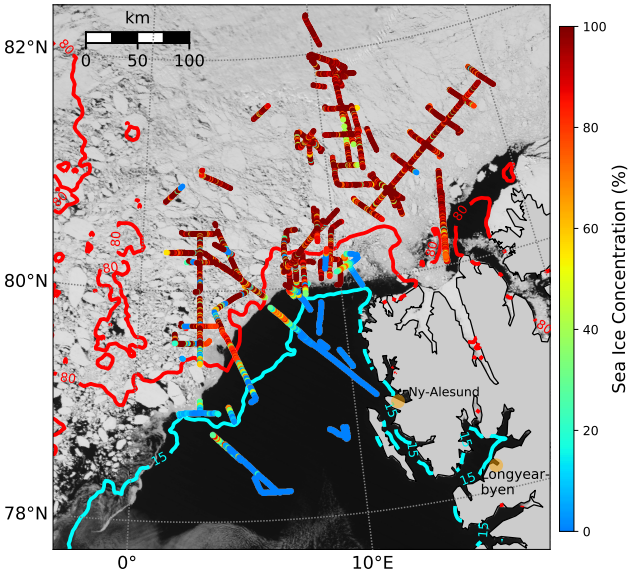

Figure 1. MODIS satellite image on 1 June 2017, representing the typical sea ice distribution during the ACLOUD campaign. All low-level flight sections during the ACLOUD campaign are indicated with the sea ice concentration derived from airborne observations. Red (80 %) and light-blue (15 %) contours indicate the campaign average sea ice concentration from daily sea ice data (Spreen et al., 2008).

information have been obtain by a Kelvin Infrared Radiation Thermometer (KT–19) (Stapf et al., 2019). The sea ice fraction (I_f) along the flight track is estimated from measurements of a digital camera equipped with a hemispheric lens. The geometrically calibrated images are obtained with a sampling frequency of 6 s from which the cosine weighted sea ice concentration was calculated (Jäkel et al., 2019). The atmospheric thermodynamic state, including air temperature and relative humidity was measured by dropsondes (Ehrlich et al., 2019a) and aircraft in situ observations (Hartmann et al., 2019) in vicinity to the low-level flight sections.

2.3 Radiative Transfer Simulations

The radiative transfer simulations for the cloud-free conditions are performed with the libRadtran package (Emde et al., 2016) using the one-dimensional plane-parallel discrete ordinate radiative transfer solver DISORT (Stamnes et al., 1988) and the molecular absorption parameterization from Kato et al. (1999) for the solar spectral range, and from Gasteiger et al. (2014) for the terrestrial wavelengths range. Daily ozone concentrations in the flight region of ACLOUD are considered and obtained from http://exp-studies.tor.ec.gc.ca/cgi-bin/selectMap. The aerosol optical thickness was neglected justified by the fact that full column aerosol information are not available for low-level flights in cloudy conditions. Therefore, the estimated CRF needs to be considered as direct aerosol plus cloud radiative forcing.

The atmospheric state, used in the radiative transfer simulations to derive the CRF, is based on radiosoundings performed in Ny-Ålesund (Svalbard) (Maturilli, 2017a, b) and onboard Polarstern (Schmithüsen, 2017), which were partly spatially and

https://doi.org/10.5194/acp-2019-534
Preprint. Discussion started: 23 July 2019

Atmospheric Chemistry and Physics Discussions

temporally separated from the airborne observations by several hundred kilometres and up to three hours. Hence, profiles from in situ measurements of temperature and relative humidity on board of both aircraft and, if available, dropsonde measurements from the Polar 5 aircraft were used to complete the local atmospheric profile data. The atmospheric levels below flight altitude were adjusted to the surface temperature measured by the KT-19.

Spectral surface albedo values have been simulated using the spectral Two-streAm Radiative TransfEr in Snow model (TARTES) (Libois et al., 2013), which is applied in a sensitivity study in section 3.4. 3D radiative transfer simulations are performed with the open-source Monte Carlo Atmospheric Radiative Transfer Simulator (MCARaTS) (Iwabuchi, 2006; Iwabuchi and Kobayashi, 2008).

3 Components of the cloud radiative forcing

3.1 Definitions

To assign processes related to single components of the surface CRF, Eq. 2 is separated in terrestrial and solar terms. The terrestrial term reads:

$$\Delta F_{\mathrm{t}} = \left(F^{\downarrow}_{\mathrm{t,cld}} - F^{\uparrow}_{\mathrm{t,cld}}\right) - \left(F^{\downarrow}_{\mathrm{t,cf}} - F^{\uparrow}_{\mathrm{t,cf}}\right). \tag{3}$$

It can be assumed to be independent of the upward irradiance ($F^{\uparrow}_{\mathrm{t,cld}} = F^{\uparrow}_{\mathrm{t,cf}}$) as a high surface emissivity enables to neglect a reflection term and for the instantaneous CRF the surface temperature is assumed to be identical for the cloudy and cloud-free case. Hence, the essential input for radiative transfer are the atmospheric temperature, the absorber gas profile and aerosol. Thus the terrestrial CRF reduces to:

$$\Delta F_{\mathrm{t}} = F^{\downarrow}_{\mathrm{t,cld}} - F^{\downarrow}_{\mathrm{t,cf}}. \tag{4}$$

The solar component of the CRF is given by:

$$\Delta F_{\mathrm{s}} = \left(F^{\downarrow}_{\mathrm{s,cld}} - F^{\uparrow}_{\mathrm{s,cld}}\right) - \left(F^{\downarrow}_{\mathrm{s,cf}} - F^{\uparrow}_{\mathrm{s,cf}}\right). \tag{5}$$

As the observations aim to quantify the local CRF, the local surface albedo α as a ratio of $F^{\uparrow}_{\mathrm{s}}$ and $F^{\downarrow}_{\mathrm{s}}$ measured during low-level flights is introduced into Eq. 5, which leads to:

$$\Delta F_{\mathrm{s}} = \left(F^{\downarrow}_{\mathrm{s,cld}} - \alpha \cdot F^{\downarrow}_{\mathrm{s,cld}}\right) - \left(F^{\downarrow}_{\mathrm{s,cf}} - \alpha \cdot F^{\downarrow}_{\mathrm{s,cf}}\right). \tag{6}$$

The three essential components for the radiative transfer, and thus, for the derivation of the solar CRF are the profiles of atmospheric thermodynamic parameters (pressure, temperature, humidity), the downward solar irradiance at the surface in cloud-free conditions ($F^{\downarrow}_{\mathrm{s,cf}}$) as well as the surface albedo α in the unobserved cloud-free conditions.
The atmospheric profile parameters modulate the downward radiation, reaching the surface in cloud-free conditions. Additionally, the surface albedo controls the multiple scattering between surface and atmosphere enhancing the downward irradiance

https://doi.org/10.5194/acp-2019-534
Preprint. Discussion started: 23 July 2019

Atmospheric Chemistry and Physics Discussions

reaching the ground over highly reflective surface-types such as snow and sea ice as compared to mostly absorbing surface like ocean water. The MIZ is characterized by strong variability in surface albedo due to the variable sea ice cover. For airborne observations close to the MIZ, as well as ground based measurements in heterogeneous terrain, horizontal photon transport is not negligible for the estimate of $F_{\mathrm{s}}^{\downarrow}$ (Ricchiazzi and Gautier, 1998; Kreuter et al., 2014). To address this problem, the downward irradiance for the cloud-free conditions and heterogeneous surface albedo needs to be simulated with an areal averaged albedo α_{ar}, also called effective albedo (Weihs et al., 2001; Wendisch et al., 2004). For example, a local surface albedo over a small lead embedded in homogeneous sea ice is not representative for the areal average surface albedo, determining the scattering processes in cloud-free conditions. To illustrate this approach, we modify Eq. 6 to:

$$\Delta F_{\mathrm{s}} = \left(F_{\mathrm{s,cld}}^{\downarrow} - \alpha \cdot F_{\mathrm{s,cld}}^{\downarrow}\right) - \left(F_{\mathrm{s,cf}}^{\downarrow}\Big|_{\alpha_{\mathrm{ar}}} - \alpha \cdot F_{\mathrm{s,cf}}^{\downarrow}\Big|_{\alpha_{\mathrm{ar}}}\right), \tag{7}$$

where $F_{\mathrm{s,cf}}^{\downarrow}\Big|_{\alpha_{\mathrm{ar}}}$ represents the downward solar irradiance at the surface simulated with the areal average albedo in cloud-free conditions.

Besides affecting the $F_{\mathrm{s}}^{\downarrow}$, the local surface albedo α in Eq. 7 changes for different illumination situations (cloudy, cloud-free) and cloud optical thickness Warren (1982). Thus, to complete the formulation of the solar CRF, the local surface albedo has to be separated in a cloudy albedo (α_{cld}) and an albedo representing the cloud-free state α_{cf}. As a result Eq. 7 reads:

$$\Delta F_{\mathrm{s}} = \left(F_{\mathrm{s,cld}}^{\downarrow} - \alpha_{\mathrm{cld}} \cdot F_{\mathrm{s,cld}}^{\downarrow}\right) - \left(F_{\mathrm{s,cf}}^{\downarrow}\Big|_{\alpha_{\mathrm{ar}}} - \alpha_{\mathrm{cf}} \cdot F_{\mathrm{s,cf}}^{\downarrow}\Big|_{\alpha_{\mathrm{ar}}}\right). \tag{8}$$

In the following sections, these three key components (thermodynamic state (section 3.2), $F_{\mathrm{s,cf}}^{\downarrow}\Big|_{\alpha_{\mathrm{ar}}}$ (section 3.3) and the impact of clouds on α_{cf} (section 3.4)) of the CRF estimate are analysed using synthetic radiative transfer simulations and illustrative ACLOUD observations, in order to quantify their separate impact on the CRF in the Arctic.

3.2 Impact of local thermodynamic atmospheric state

In the MIZ, the thermodynamic state of the atmosphere changes within short distances due to the influence of the surface on the airmass (warm air moving north over cold sea ice, cold air moving south over warm open ocean) (Lampert et al., 2012). In this case, differences in the collocation of airborne in situ measurements of atmospheric profiles and low-level flights might be significant and effect the radiative transfer simulations, and thus, the local CRF estimate. Exemplarily, the spatial variability of air temperature profiles measured on 2 June 2017 by the aircraft instruments (Polar 6) and dropsondes is illustrated in Fig. 2a. The synoptical situation during this flight (west of Svalbard) was characterized by warm air advection with optically thick clouds moving from the open ocean over the MIZ. The consecutive in situ profiles illustrate the changes in inversion height along the flight leg, which changed from roughly 800 m over the ocean to 250 m over the sea ice within 50 to 100 km. The relative humidity (not shown here) changed accordingly.

For all profiles, radiative transfer simulations have been run to calculate $F_{\mathrm{s,cf}}^{\downarrow}$ and $F_{\mathrm{t,cf}}^{\downarrow}$ for the cloud-free reference case. The surface albedo and SZA were fixed to 0.8 and 60°, respectively. Fig. 2b shows the simulated downward irradiance and corresponding values of the solar and terrestrial CRF. While terrestrial irradiance increases with increasing humidity and

https://doi.org/10.5194/acp-2019-534
Preprint. Discussion started: 23 July 2019

Atmospheric Chemistry and Physics Discussions

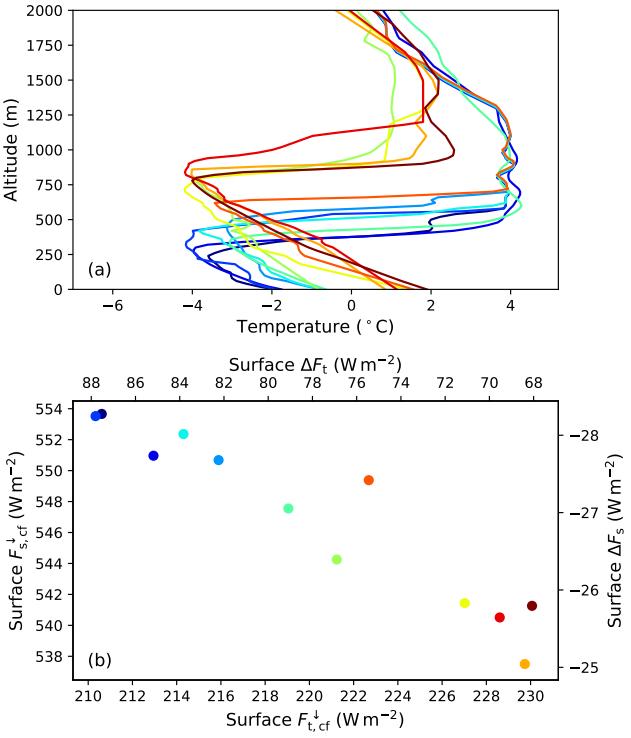

Figure 2. (a) Temperature profiles observed during the warm air intrusion on 2 June 2017. The profiles are obtained from dropsonde and in situ measurements (merged with radiosoundings) and are color-coded by the air temperature in the lowest 200 m. (b) Correlation between simulated cloud-free $F_s^{\downarrow}$ and $F_t^{\downarrow}$ assuming the observed atmospheric profiles from (a) (same color code). The second x and y axis estimates the expected terrestrial/solar CRF at the surface by assuming a constant $F^{\downarrow}_{s,cld}$ (412 W m^{-2}) and $F^{\downarrow}_{t,cld}$ (298 W m^{-2}) based on observations. For the simulations the surface albedo was fixed to 0.8 and the SZA to 60°.

temperature (enhanced emission), the solar irradiance decreases (enhanced scattering and absorption). The CRF for each case is estimated using the average observed $F^{\downarrow}_{s,cld}$ and $F^{\downarrow}_{t,cld}$ during the low-level section on 2 June 2017. The results show a strong variability in ΔF induced by changes in the thermodynamic structure. The relative deviations range up to 29 % for the terrestrial and 11 % for the solar CRF, which highlights that neglecting changes of the atmospheric thermodynamic state within a few kilometers can cause significant errors in the retrieved CRF. Especially for airmass transformation like warm air intrusions and cold air outbreaks in the Arctic (Pithan et al., 2018), this is a relevant issue.

Another aspect regarding the thermodynamic state of the atmosphere is the impact of the average aircraft flight altitude (here 80 m) on the estimate of CRF. The $F^{\downarrow}_{t,cf}$ is simulated for local flight altitude and not exactly for the surface. Due to the fact that the vertical gradient $dF_t^{\downarrow}/dz$ below clouds remains almost the same in the cloudy and cloud-free state, the observed CRF in flight altitude can be safely related to surface CRF values. For an interpretation of single terrestrial irradiance directions (not shown in this study) and a comparison to surface observations, changes due to prevailing near-surface temperature profile have to be expected.

https://doi.org/10.5194/acp-2019-534
Preprint. Discussion started: 23 July 2019

Atmospheric Chemistry and Physics Discussions

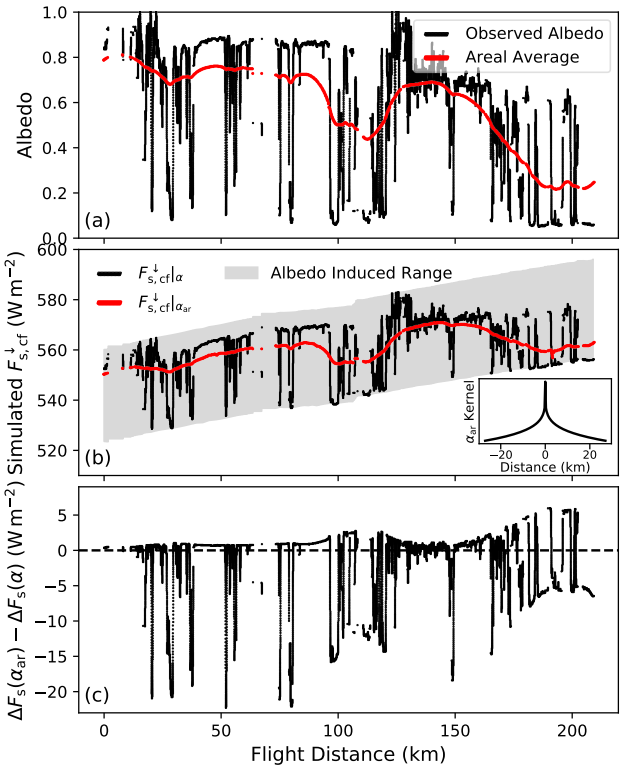

Figure 3. Time series (covered distance) of measured broadband surface albedo (black) (a) and simulated $F^{\downarrow}_{\mathrm{s,cf}}$ (b) along the low-level flight track during the 23 May 2017. The red line in (a) shows the areal averaged albedo using the kernel embedded in (b). (b) The gray area shows the potential variability of $F^{\downarrow}_{\mathrm{s,cf}}$ due to surface albedo changes. The black and red scatter shows the $F^{\downarrow}_{\mathrm{s,cf}}\big|_{\alpha}$ and $F^{\downarrow}_{\mathrm{s,cf}}\big|_{\alpha_{\mathrm{ar}}}$ respectively. (c) Difference in solar CRF estimate between $\Delta F_{\mathrm{s}}(\alpha_{\mathrm{ar}})$ and $\Delta F_{\mathrm{s}}(\alpha)$.

3.3 Impact of areal versus local surface albedo

In Fig. 1 the variability of the observed sea ice fraction I_{f} can directly be related to the heterogeneous surface albedo distributions in the MIZ. For the observations carried out on 23 May 2017, the measured broadband surface albedo along the flight track is shown in Fig. 3a. The low-level section started in the MIZ over large ice floes and small leads and ended over the open ocean in vicinity of the ice edge with occasionally scattered sea ice floe fields. Leads with the size of a few tens of meters up to a few kilometers caused a highly variable local surface albedo. In Fig. 3b the simulated $F^{\downarrow}_{\mathrm{s,cf}}$ using the observed 20 Hz surface albedo illustrates the problem of albedo heterogeneity. Without an appropriate smoothing the simulated $F^{\downarrow}_{\mathrm{s,cf}}$ would change on small horizontal scale by up to 35 $\mathrm{W\,m^{-2}}$ (SZA average: 59.2°) within the range of $F^{\downarrow}_{\mathrm{s,cf}}$ influenced by multiple scattering indicated by the gray shaded area in Fig. 3b. Therefore, the downward irradiance for the cloud-free conditions, required for Eq. 8, needs to be simulated with an appropriate areal averaged albedo.

For the low-level flights during ACLOUD a moving average filter using a kernel with the shape similar to a Laplace-distribution

https://doi.org/10.5194/acp-2019-534
Preprint. Discussion started: 23 July 2019

Atmospheric Chemistry and Physics Discussions

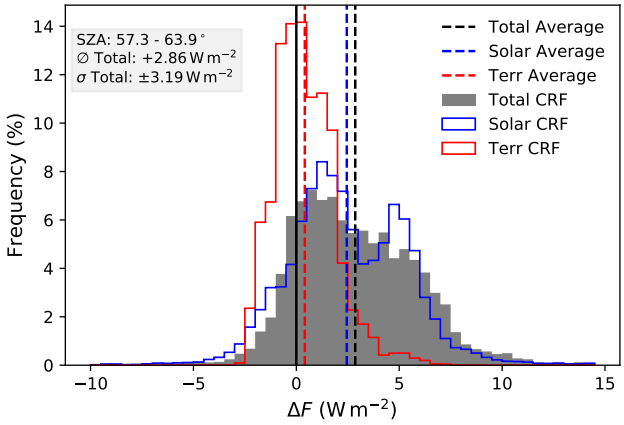

Figure 4. Histogram of solar, terrestrial and total ΔF derived during the cloud-free ACLOUD flight on 25 June 2017. Statistics are given in the gray box (mean ∅, standard deviation σ).

was applied to estimate the areal averaged surface albedo. The filter shape and width was estimated by 3D radiative transfer simulations of a typical scenario where leads of different sizes are embedded in homogeneous sea ice (not shown here). The simulated irradiance of the 3D model output over the heterogeneous surface albedo field was reproduced by 1D simulations by applying the filter embedded in Fig. 3b to the albedo field and using the obtained effective albedo for the 1D model. This rather large filter width indicates, that small leads of up to 1km embedded in sea ice show a minor impact. Applying the moving average kernel to the observed local albedo results in the areal averaged albedo, shown in Fig. 3a and the simulated $\Delta F_{\mathrm{s}}(\alpha_{\mathrm{ar}})$ (Fig. 3b), which follows the large scale trends of surface albedo but mitigates small scale fluctuations.

Neglecting these effects would result in uncertainties of the local solar CRF estimate, as shown in Fig. 3c. On average, the effect for flight section in Fig. 3 is of minor importance (average -2 $\mathrm{W\,m^{-2}}$), because under- and overestimation of solar CRF cancel in this example, similar to results from Benner et al. (2001). Nevertheless, on a local scale the difference between the two approaches reaches values between -22 $\mathrm{W\,m^{-2}}$ over open water in the vicinity of ice floes, where the $F^{\downarrow}_{\mathrm{s,cf}}$ would be underestimated by applying the local albedo, and +6 $\mathrm{W\,m^{-2}}$ in scattered ice floe fields in the ocean with an overestimation of $F^{\downarrow}_{\mathrm{s,cf}}$. Hence, the uncertainties and potential noise is limited, which enables a more reliable estimate of the CRF in the MIZ.

During ACLOUD a flight in cloud-free conditions on 25 June 2017 was used for a comparison between measured and simulated irradiances to estimate the accuracy of this dataset. The difference between observed and simulated $F^{\downarrow}_{\mathrm{cf}}$ for the low level flights of both aircraft (2.1 hours of data) was 6.5±7.3 $\mathrm{W\,m^{-2}}$ (1.2 %) in the solar and 0.41±1.45 $\mathrm{W\,m^{-2}}$ (0.2 %) in the terrestrial irradiance. The histograms of the CRF for that day are shown in Fig. 4. The mean values of the entire flight section was 2.45 $\mathrm{W\,m^{-2}}$ in the solar and 0.41 $\mathrm{W\,m^{-2}}$ in the terrestrial. The slightly positive CRF might be caused by the upper air sounding approximately 300 km in the south of the flight track or the aerosol conditions (aerosol optical thickness was set to zero in the simulation). Additionally to measurement uncertainties, the radiative transfer modelling can induce a bias in the solar wavelength ranges (Randles et al., 2013). Due to the absence of cloud-free conditions during other low-level flights of

https://doi.org/10.5194/acp-2019-534
Preprint. Discussion started: 23 July 2019

Atmospheric Chemistry and Physics Discussions

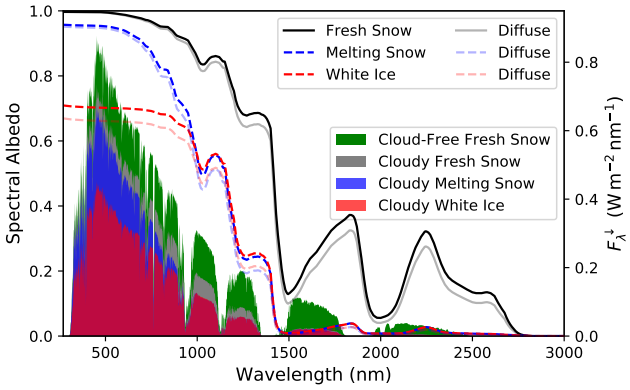

Figure 5. Spectral snow albedo of three seasonal sea ice types for different SSA and snow thickness above sea ice with spectrally neutral albedo of 0.5. Non attenuated lines show the albedo of the cloud-free situations (SZA of 65°), attenuated lines the albedo for overcast conditions. The downward irradiance (right y-axis) simulated for these cases are exemplary shown by the shaded areas. Green shows the cloud-free spectra over fresh snow, gray, blue and red under cloudy conditions (LWP of 80 $\mathrm{g\,m^{-2}}$) for the surface albedo related by the colors.

the ACLOUD campaign this comparison can be considered as a rough estimate of potential uncertainties during the whole ACLOUD campaign.

3.4 Impact of clouds on the surface albedo

The effect of clouds on the broadband surface albedo, implemented in Eq. 8, is analysed by a set of spectral albedos of three sea ice types common in the Arctic for different seasons. Different snow packs with a density of 300 $\mathrm{kg\,m^{-2}}$ are specified with various values of snow geometric thickness and specific surface area (SSA) and located above a layer representing bare sea ice with a wavelength constant broadband albedo of 0.5. Fresh cold and dry snow (SSA = 80 $\mathrm{m^2\,kg^{-1}}$, 20 cm thick) represents early to late spring conditions, melting snow (SSA = 5 $\mathrm{m^2\,kg^{-1}}$, 20 cm thick) the melting season in late spring early summer, and thin melting snow/white ice (SSA = 5 $\mathrm{m^2\,kg^{-1}}$, 1 cm thick) summer conditions, before the melt pond formation. The spectral albedo for each type was simulated with the TARTES model for 65° SZA; the respective results are shown in Fig. 5 (solid lines) together with simulated downward irradiances from the atmospheric radiative transfer simulations using libRadtran (shaded spectra).

The general impact of snow properties on the spectral albedo is characterized by stronger absorption at longer wavelengths with decreasing SSA (increasing effective grain size) and can be seen by comparing the albedo of fresh and melting snow in Fig. 5. A decreasing SSA amplifies the contrast between shorter and longer wavelength. A thinning of the snow layer or impurities in snow enhance the absorption mainly in the shorter visible wavelength range, as illustrated by the albedo of melting snow in comparison to that of white ice.

Two processes influencing the broadband snow albedo are related to the transition from cloud-free to cloudy atmospheric con-

https://doi.org/10.5194/acp-2019-534
Preprint. Discussion started: 23 July 2019

Atmospheric Chemistry and Physics Discussions

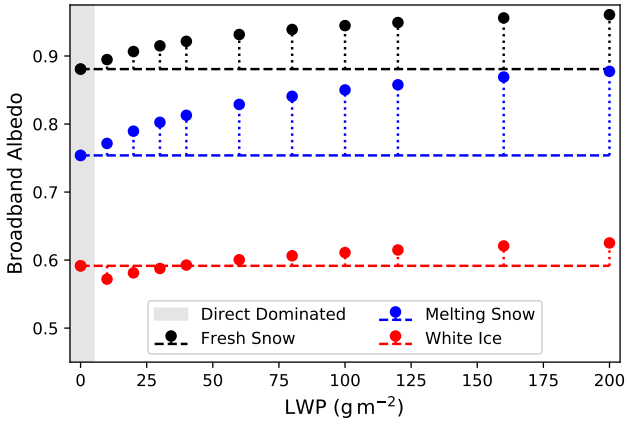

Figure 6. Broadband albedo integrated from simulated up- and downward spectral irradiance as a function of cloud LWP using the color-related spectral albedos of Fig 5. The approximate area of direct dominated/ cloud free radiation is indicated by the gray shading (SZA of 65°). The horizontal line indicates the cloud-free albedo as a reference.

ditions. In an overcast atmosphere with clouds of sufficient optical thickness, mainly diffuse radiation illuminates the surface as compared to cloud-free conditions, when the direct solar radiation dominates. In the Arctic, large values of SZA ($> 50°$) are common. In overcast conditions, scattering processes in clouds decrease the averaged incoming (effective) angle of the mainly diffuse irradiance to approximately 50° above snow (Warren, 1982). With decreasing effective SZA, the penetration depths of photons into the snow and ice surface increases, enhancing the probability of absorption, and thus decrease the overall broadband surface albedo (Warren, 1982). In Fig. 5 this effect is illustrated by the attenuated lines representing the respective diffuse albedo values. Compared to the surface albedo in cloud-free atmospheric conditions of fresh snow the change of effective SZA (in this example from 65° to approximately 50° SZA) causes a lower spectral surface albedo, especially in the non-visible wavelength range, while the highly reflective visible wavelengths are not affected. The downward solar irradiance spectra, exemplarily shown for cloudy conditions with LWP of 80 $\mathrm{g\,m^{-2}}$ (gray shaded area in Fig. 5), indicate that the main part of $F_s^{\downarrow}$ (shorter wavelengths) is not affected by this change and a weak impact on the broadband albedo is expected for fresh snow. For albedo values characterized by stronger absorption in the visible wavelength range (albedo of white ice, red line in Fig. 5), a stronger change between direct-dominated and diffuse broadband albedo is expected.

Besides the changing effective SZA, clouds reduce the incident irradiance by attenuating especially in the near-infrared wavelength range (Grenfell and Perovich, 2008). With increasing cloud optical thickness the spectral slope of downward irradiance is imprinted in the surface spectra, which can be seen in Fig. 5 by comparing the green shaded (cloud-free) and the gray shaded (cloudy) spectrum. The spectral albedo of ice and snow is higher for short wavelengths resulting in a increasing wavelength-integrated (broadband) surface albedo with increasing cloud optical thickness. This effect becomes the stronger the more pronounced the slope between visible and near-infrared wavelength becomes, which can be induced by two processes: either stronger absorption by clouds due to a higher LWP, or by spectral changes in the albedo. With decreasing SSA, transition

https://doi.org/10.5194/acp-2019-534
Preprint. Discussion started: 23 July 2019

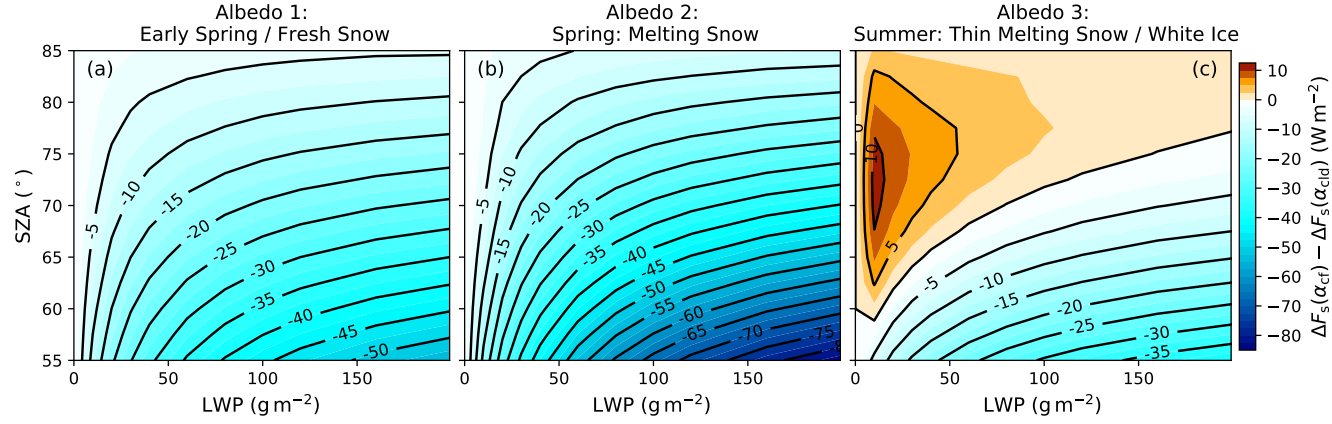

Figure 7. Bias of the solar CRF ($\Delta F_s(\alpha_{cf}) - \Delta F_s(\alpha_{cld})$) caused by neglecting the change between observed cloudy and cloud-free surface albedo as a function of cloud LWP and SZA. The three albedo types from Fig. 5 have been assumed, (a) fresh snow representative for early spring, (b) melting snow during late spring, and (c) thin melting snow/white ice found in early summer.

from fresh to melting snow, more radiation is absorbed in the near-infrared (compare black and blue lines in Fig. 5), which affects $F_s^{\downarrow}$ (grey and blue shaded spectra). For the spectral albedo of white ice (red shaded area) the slope in the spectra is less pronounced, and a weaker increase of broadband albedo is expected for increasing LWP.

For all three surface albedo types shown in Fig. 5, the effect of clouds on the broadband surface albedo (as a function of LWP) is presented in Fig. 6 for a SZA of 65°. The gray area indicates the direct-dominated radiation in cloud-free conditions; dashed lines represent the cloud-free value as a reference. In general, the lower the ratio of spectral albedo between shorter and longer wavelengths, the stronger is the increase of broadband albedo with increasing LWP, exemplary shown for the black and blue scatter in Fig. 6 representing fresh and melting snow, respectively. Spectral absorption of the surface in shorter wavelengths strongly decreases the broadband albedo, but it will also alter the behaviour with increasing LWP (Fig. 6, red). For low LWP values, the broadband albedo is lower compared to cloud-free conditions due to a significant lower spectral diffuse albedo (dashed and attenuated dashed red in Fig. 5) at shorter wavelengths. However, with increasing LWP the weighting effect in transmitted $F_s^{\downarrow}$ to shorter wavelength compensates/dominates and, as a consequence, it increases the broadband surface albedo compared to cloud-free conditions.

3.4.1 Albedo-cloud interaction and CRF

In calculations of the CRF based on measurements, the observed surface albedo below clouds commonly serves as a reference for the simulations of $F_{s,cf}^{\downarrow}$ and calculation of ΔF_s. Also weather and climate models, where the change of the broadband albedo with increasing LWP are not or only poorly parameterized, may have a bias in the estimated CRF. To estimate the significance of this effect, radiative transfer simulations have been used to calculate the solar CRF, either assuming the correct cloud-free albedo or the wrong cloudy albedo. The difference $\Delta F_s(\alpha_{cf}) - \Delta F_s(\alpha_{cld})$ between both runs, and thus, an underestimate of

https://doi.org/10.5194/acp-2019-534
Preprint. Discussion started: 23 July 2019

Atmospheric Chemistry and Physics Discussions

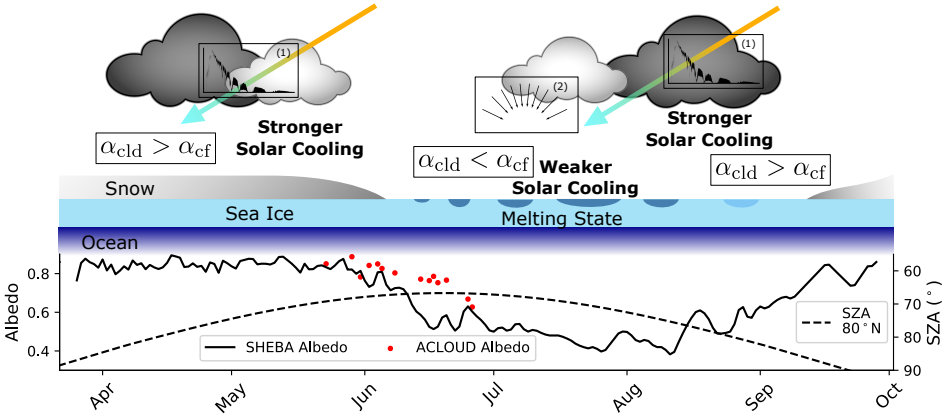

Figure 8. Hypothetical scheme of the seasonal cycle of surface albedo-cloud interaction related modification of solar CRF. Dominant processes influencing the transition from cloudy to cloud-free surface albedo in the specific season are represented by the icons (1, weighting of downward irradiance to shorter wavelength with increasing LWP) and (2, transition from direct to diffuse radiative transfer). The seasonal cycle of surface broadband albedo is shown by SHEBA observations (200 m albedo line). Averaged ACLOUD observations for homogeneous sea ice ($I_f > 95\,\%$) are shown in red. Computed daily averaged SZA for 80° N in dashed black.

the solar cooling effect if the cloudy albedo is used, are shown in Fig. 7 as a function of SZA and LWP. Negative (bluish) values indicate a stronger solar cooling effect for $\Delta F_s(\alpha_{cf})$. The simulations have been performed for all three sea ice types in Fig. 5 and changes in direct/diffuse radiation due to SZA have been taken into account.

In case of snow surfaces, influenced by the SSA (Fig. 7a and b), the cooling effect of clouds on the surface is underestimated (blue colors), if the cloudy albedo is used to derive the solar CRF. In general, the lower the SZA and the higher the LWP, the stronger the underestimation of the cooling effect becomes. Additionally, the coarser the snow grains (melting snow) the stronger the underestimation. In contrast, during summer and for thin melting snow or white ice (Fig. 7c), the cooling effect is overestimated for low sun and optically thin clouds, if the apparent cloudy albedo is used for ΔF_s, and shifts towards the underestimation for optically thick clouds and/or lower SZA.

The values of under-/overestimation indicate that the surface albedo-cloud interaction might significantly impact the estimate of solar CRF. Especially for clouds over snow, the cooling effect of clouds is considerably larger. Due to the dependence of spectral surface albedo shapes, a seasonal dependence of this surface albedo-cloud interaction, and thus, the solar CRF, is indicated.

In Fig. 8 a hypothetical scheme of the modified seasonal cycle of CRF due to the surface albedo-cloud interaction, is proposed. The time series of surface albedo as observed during the SHEBA campaign is shown to illustrate the seasonal transition as reported by Perovich et al. (2002). During spring, early summer and autumn surface albedos related to snow on sea ice are found. The results from Fig. 7 indicate that the shift of transmitted irradiance towards shorter wavelength (process 1 in Fig. 8) is dominant in these situations and clouds induce a stronger cooling effect on the surface. With the beginning of the melting season, the change between diffuse and direct albedo will dominate (process 2) for optical thin clouds and high SZA, potentially

https://doi.org/10.5194/acp-2019-534
Preprint. Discussion started: 23 July 2019

Atmospheric Chemistry and Physics Discussions

reducing the cooling effect on the surface. In this period the onset of melting (rapidly decreasing albedo), the melt pond fraction, and the SZA (dashed black line in Fig. 8) critically influences the sign of this modification. For the ACLOUD campaign, snow on ice was the dominant surface type (Jäkel et al., 2019), which explains the slightly later decrease in surface albedo (Fig. 8, red line) compared to SHEBA data (black) and represents the transition from cold and fresh snow to melting snow. Transferred to the results from Fig. 7 a stronger cooling effect should be expected during ACLOUD. Though, conclusions about the yearly impact on the estimate of solar forcing are not yet possible, as coupled surface-atmosphere radiative transfer models capable of representing surface types like melt ponds are required to study the full seasonal cycle of solar CRF influence by surface albedo-cloud interactions.

4 Cloud radiative forcing during ACLOUD

The problems of calculating the CRF, as discussed in sections 3.2, 3.3 and 3.4 are considered in the data processing of the ACLOUD measurements. Therefore, the closest available atmospheric profile was applied in the radiative transfer simulations as well as the areal averaged surface albedo, required for the simulations of $F^{\downarrow}_{\mathrm{s,cf}}$, has been calculated for the low-level flights. The final step is to retrieve the local surface albedo under cloud-free atmospheric conditions from the observed cloudy-sky albedo, in order to obtain a more realistic estimate of the CRF.

4.1 Retrieving the cloud-free albedo from cloudy-sky observations

To obtain an estimate of the cloud-free albedo, the broadband albedo parameterization developed by Gardner and Sharp (2010) for snow and ice surfaces was applied. Gardner and Sharp (2010) considered the dependence of broadband albedo with respect to SZA, SSA, concentration of absorbing carbon, as well as the cloud optical thickness. The parameterization is valid for homogeneous snow and ice including a cloud optical thickness below 30 (LWP of 133 $\mathrm{g\,m^{-2}}$ for an effective cloud droplet radius $r_{\mathrm{eff}} = 8\,\mu\mathrm{m}$). During ACLOUD, the observed albedo ranged between 0.9 for homogeneous sea ice covered with snow and values below 0.6 during the melting season (Wendisch et al., 2019; Jäkel et al., 2019). To include these data in the analysis and cover this albedo range only as a function of grain size (SSA), an impurity load of absorbing carbon of 0.1 ppmw was chosen, which causes a similar spectral behaviour of the albedo as changes in snow thickness. As shown by Jäkel et al. (2019), snow overlaying sea ice was the predominant surface type over closed sea ice during ACLOUD. Nevertheless, the potential variability in the spectral surface albedo with respect to absorption in the short wavelength ranges during the campaign is only roughly covered by this approach and needs to be considered in the interpretation of the obtained albedo values.

The parameterization is used to generate lookup tables, as a function of observed variables of cloudy-sky albedo, LWP and local SZA. Isolines of SSA are used to extrapolate the cloud-free albedo (LWP = $0\,\mathrm{g\,m^{-2}}$). To apply the albedo parameterization by Gardner and Sharp (2010) the cloud optical thickness or LWP is required. As the cloud properties change on small horizontal scales, a retrieval of LWP based on the airborne measurements of cloud transmissivity was used, which is described in the appendix A.

https://doi.org/10.5194/acp-2019-534
Preprint. Discussion started: 23 July 2019

Atmospheric Chemistry and Physics Discussions

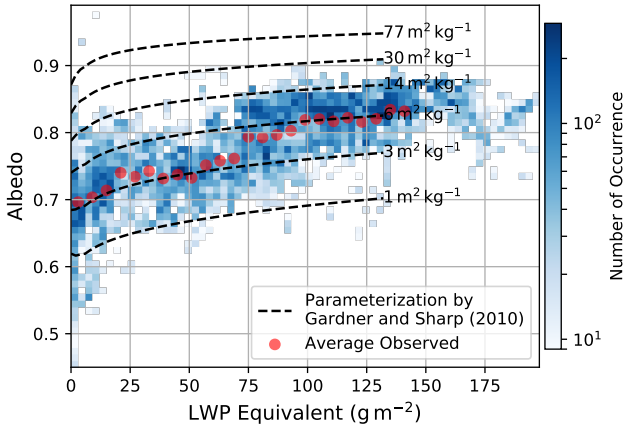

Figure 9. Relation between broadband albedo and retrieved LWP equivalent observed on 14 June 2017 ACLOUD over homogeneous sea ice ($I_f > 98\,\%$). The broadband albedo parameterization by Gardner and Sharp (2010) is shown for different SSA and the average SZA by dashed lines (impurity load of 0.1ppmw). Averaged observations ($6\,g\,m^{-2}$ bins) are shown in red scatter.

4.1.1 Application to the observations

The dependence of the surface albedo on the cloud LWP is shown in Fig. 9 as measured over homogeneous sea ice ($I_f > 98\,\%$) on 14 June 2017. Additionally, the albedo parameterization by Gardner and Sharp (2010) for the averaged SZA (63.7°) and different values of SSA is shown. During 1.7 hours of low-level flights below clouds, a large area was mapped (80.7-81.8° N,9.8-12.7° E) and a strong variability in optical thickness including occasional openings with direct illumination of the surface and optical thick multilayer clouds was covered. The surface temperatures were close to zero, indicating the beginning melting season (Jäkel et al., 2019). The observed albedo values averaged for $6\,g\,m^{-2}$ bins (dashed red in Fig. 9) change from 0.7 for low values of LWP to 0.83 for a LWP larger than $100\,g\,m^{-2}$. While the overall trend of increasing albedo with increasing LWP is represented, the slope follows the parameterization for a SSA between $3\,m^2\,kg^{-1}$ (1 mm) for lower LWP values and $6\,m^2\,kg^{-1}$ (0.5 mm) for higher LWP. This effect might be related to different observed cloud and surface areas as the distribution includes data from both aircraft.

Extrapolating the observations (pair of variates) of LWP equivalent and surface albedo along isolines of SSA to a LWP of zero gives an estimate of the cloud-free surface albedo. For the example given here, for an α_{cld} of 0.82 and LWP of $100\,g\,m^{-2}$ a cloud-free albedo of 0.74 would be estimated, and thus, 0.06 lower than the observed one in overcast conditions. Due to the non-linear increase of α_{cld} with LWP the potential error induced by uncertainties in the retrieved LWP is larger for lower LWP and additionally depends on the prevailing surface types. For LWP values exceeding the limitation of the parameterization the maximum valid LWP was applied.

A comparison of measured (overcast) α_{cld} and extrapolated cloud-free albedo α_{cf} is shown in Fig. 10a. The frequency distributions are calculated for all low-level flights during ACLOUD over homogeneous sea ice ($I_f > 98\,\%$). The broad distribution

https://doi.org/10.5194/acp-2019-534
Preprint. Discussion started: 23 July 2019

Atmospheric Chemistry and Physics Discussions

of observed albedo illustrates the seasonal transition of sea ice properties from a cold period end of May 2017 into the melting season in June 2017 (Wendisch et al., 2019; Jäkel et al., 2019). On average, the overcast albedo was about 0.8. The estimated cloud-free albedo gives an average value of 0.74, which is approximately 6 % lower than α_{cld}. The distribution of α_{cf} is slightly narrower than measured in cloudy conditions, because the majority of cloud-free flight sections takes place close to the end of the campaign with low values of surface albedo, and thus, give a lower bound to the distribution.

Fig. 10a shows only measurements conducted over homogeneous sea ice, which was frequently observed during ACLOUD. In the MIZ, though, the heterogeneous sea ice and the corresponding reduced surface albedo prevents an application of the original parametrization by Gardner and Sharp (2010). However, making use of the cosine weighted sea ice fraction I_{f} and its linear relation to the albedo, changes due to the surface albedo-cloud interaction can be scaled to the prevailing I_{f} by assuming diffuse radiative transfer (Lambertian albedo),

$$\alpha(I_{\mathrm{f}}) = (\alpha - \alpha_{\mathrm{w}}) \cdot I_{\mathrm{f}} + \alpha_{\mathrm{w}}, \tag{9}$$

with $\alpha_{\mathrm{w}} = 0.07$ (average open ocean albedo during ACLOUD). Below an I_{f} of 10 % no correction have been applied because the cloud effect on the surface albedo can be neglected.

4.2 Correction of CRF

To illustrate the effect of surface albedo-cloud interactions on the calculation of the CRF during the ACLOUD campaign, the CRF was computed using both measured cloudy albedo (α_{cld}) and the estimated cloud-free albedo (α_{cf}). Fig. 10b shows the frequency distribution of the solar CRF for both solutions, observed over homogeneous sea ice ($I_{\mathrm{f}} > 98$ %). The CRF based on the observed albedo (gray bars) shows a bimodal distribution. The mode around 0 $\mathrm{W\,m^{-2}}$ represents cloud-free situations and heterogeneous optically thin clouds, where 3D effects induced occasionally positive solar CRF values as reported in Wendisch et al. (2019). The broader mode between -60 $\mathrm{W\,m^{-2}}$ and -20 $\mathrm{W\,m^{-2}}$ characterizes the cloudy mode as a function of the prevailing surface albedo and LWP. Applying the estimated cloud-free albedo (red histogram in Fig. 10a), shifts the solar CRF in Fig. 10b of the cloudy mode to more negative values, indicating a stronger cooling effect. The non-linearity in the functional dependence of the solar CRF and surface albedo spreads the frequency distribution, while the mode for cloud-free conditions is not affected.

In total the solar CRF showed on average a weak cooling effect of -33 $\mathrm{W\,m^{-2}}$ using the observed albedo values under cloudy conditions (LWP > 1 $\mathrm{g\,m^{-2}}$). Applying the correct surface albedo for cloud-free conditions almost doubles the solar cooling effect to -63 $\mathrm{W\,m^{-2}}$. These values hold for the ACLOUD observations with an average LWP during cloudy conditions over sea ice of 58 $\mathrm{g\,m^{-2}}$ and a SZA of 59°. In combination with the distribution of the terrestrial CRF (blue histogram in Fig. 10b), which averages to 69 $\mathrm{W\,m^{-2}}$ in cloudy conditions, the total (solar plus terrestrial) CRF estimate (Fig. 10c) shifts from a significant warming effect of 37 $\mathrm{W\,m^{-2}}$ over sea ice to an in average almost neutral effect (6 $\mathrm{W\,m^{-2}}$). Also the distribution of the corrected CRF indicates that during the end of the campaign already the cooling effect was dominant (uncorrected mainly positive). Considering that the predominant surface type of the campaign was still sea ice covered by snow, the transition from

https://doi.org/10.5194/acp-2019-534
Preprint. Discussion started: 23 July 2019

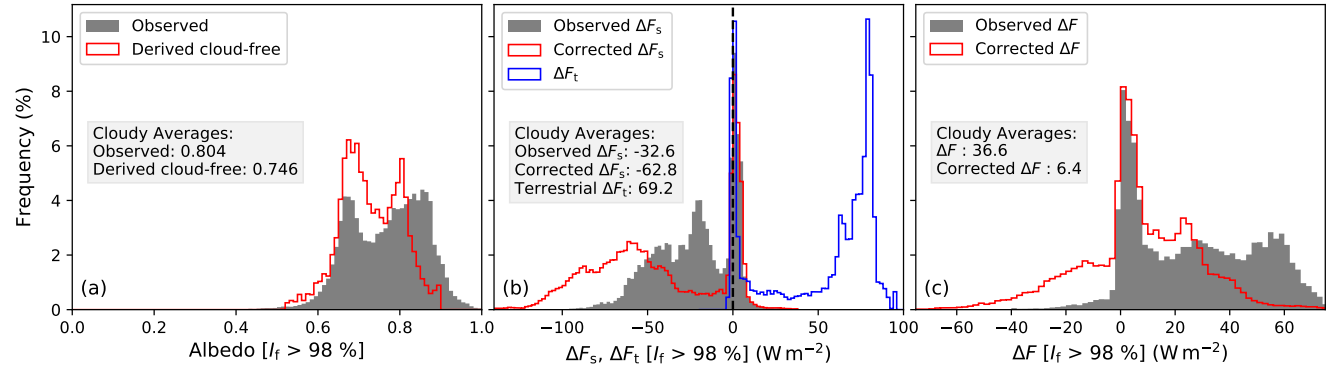

Figure 10. (a) Frequency distribution of the observed (gray) and cloud-free estimated (red) surface albedo for all ACLOUD measurements obtained over homogeneous sea ice ($I_f > 98\,\%$). (b) Terrestrial (blue) and solar CRF using the observed albedo (gray) and the solar CRF applying the estimated cloud-free albedo (red). (c) The total (solar + terrestrial) CRF calculated with both albedo estimates are shown in panel (c). Average values for cloudy conditions (LWP > 1 g m^{-2}) are given in the embedded text boxes of each panel.

warming to cooling effect of clouds could already start early in the season, before the formation of melt ponds and the rapid drop in surface albedo, which underlines the potential impact of surface albedo-cloud interactions.

5 Conclusions

To estimate the instantaneous warming or cooling effect of clouds on the surface REB from observations or models, a precise knowledge of the cloud-free state is indispensable.

Especially in the transition region between open ocean and closed sea ice (the MIZ) the thermodynamic state of the atmosphere changes on horizontal scales of a few kilometers, which significantly influences the simulated cloud-free radiative field. To obtain reliable information of CRF related to airmass transformations like warm air intrusions or cold air outbreaks in the Arctic (Tjernström et al., 2015; Pithan et al., 2018), high temporal and spatial resolution is required to obtain reliable values of local CRF induced by these large scale processes.

Variability in sea ice concentration is closely linked with fluctuations in the local surface albedo. The derivation of cloud-free downward irradiance in these condition requires an estimate of the effective areal average surface albedo, determining the multiple scattering on large scales. Moving average filters with shapes appropriate of reproducing 3D radiative transfer need to be applied to obtain a reliable local solar CRF.

The transition between cloudy and cloudy-free atmospheric states is accompanied by changes in the radiative transfer, affecting the surface albedo, and thus, the CRF. Combining spectral snow surface albedo models with atmospheric radiative transfer models enables to quantify the impact of two processes related to spectral surface albedo-cloud interactions. The weighting effect of downward irradiance appears to be dominant for snow surfaces and enhances the cooling effect of clouds on the surface. For the second process, a change between direct dominated radiation in the cloud-free state and diffuse radiation in

https://doi.org/10.5194/acp-2019-534
Preprint. Discussion started: 23 July 2019

Atmospheric Chemistry and Physics Discussions

the cloudy state, the sign of the modification depends on SZA, cloud optical thickness and the melting state of sea ice.

For the ACLOUD campaign, characterized by snow on sea ice in the beginning melting season, the averaged solar CRF estimate over homogeneous sea ice of -33 $\mathrm{W\,m^{-2}}$ (cooling) almost doubled when surface albedo-cloud interactions were taken into account (-63 $\mathrm{W\,m^{-2}}$). The campaign averaged total CRF was thereby shifted from a mainly warming effect of clouds over sea ice to an on average almost neutral effect, for the ACLOUD observations with low SZA. Hence, the observed albedo trend during the campaign (Fig. 8) induced a transition in CRF from a warming to a cooling already for snow covered surface types, and thus, earlier in the season. This indicates a potential prolongation of the period in which clouds are expected to have a cooling effect on the surface and highlights the impact of surface albedo-cloud interactions and a required reassessment of the CRF in the Arctic. Long-term measurements such as those performed during the SHEBA campaign or planned within the Multidisciplinary drifting Observatory for the Study of Arctic Climate (MOSAiC) expedition (www.mosaic-expedition.org), with an appropriate instrumentation and radiative transfer modelling will be required to quantify these effects and its potential seasonal dependence.

Besides observation, also global climate models and their estimate of the cloud radiative feedback are based on the impact of clouds on the surface REB, for which the surface albedo is fundamental. For specific surface types often fixed values of broadband surface albedo are assigned and modulated by temperature dependences. However, these simplified parameterizations are not capable of describing surface albedo-cloud interactions. The use of parameterizations accounting for these effects like the one from Gardner and Sharp (2010) are necessary and highlight the need for coupled surface atmosphere models with represented surface microphysical properties.

Further effort in coupled surface atmosphere radiative transfer modelling with a representation of common surface albedos like the ones from melt ponds in the Arctic are required to track the true seasonal cycle of solar CRF. Spectral albedo observations combined with the common broadband devises would help to account for the spectral features in surface albedo and trace changes in SSA. The proposed approach of reproducing the cloud-free albedo can not adequately reflect the diversity of spectral surface albedos and issues related to the surface albedo-cloud interaction, especially in summer.

Considering the surface albedo-cloud interaction in global climate models and upcoming long-term observations such as MOSAIC will further improve our understanding of CRF and cloud radiative feedback in the Arctic environment and its role for Arctic amplification.

Data availability. The pyranometer and pyrgeometer broadband irradiance and KT-19 nadir brightness temperature from AWI aircraft Polar 5&6 during the May to June 2017 ACLOUD campaign are published on the PANGAEA database (Stapf et al., 2019). Air temperature, relative humidity and pressure in situ profiles from both aircraft are used from (Hartmann et al., 2019). Polar 5 Dropsondes: (Ehrlich et al., 2019a). Calibrated fisheye camera images: (Jäkel and Ehrlich, 2019; Jäkel et al., 2019). Radiosoundings from Polarstern (Schmithüsen, 2017) and Ny-Ålesund (Maturilli, 2017a, b).

https://doi.org/10.5194/acp-2019-534
Preprint. Discussion started: 23 July 2019

Atmospheric Chemistry and Physics Discussions

Appendix A: Transmissivity based retrieval of LWP equivalent

The cloud transmissivity is defined by the ratio of measured $F^{\downarrow}_{\mathrm{s,cld}}$ and the simulated cloud-free $F^{\downarrow}_{\mathrm{s,cf}}$ downward irradiance:

$$\mathcal{T} = \frac{F^{\downarrow}_{\mathrm{s,cld}}}{F^{\downarrow}_{\mathrm{s,cf}}}. \tag{A1}$$

$\mathcal{T}$ can be converted into cloud optical thickness or LWP, however, it is important to account for the surface albedo dependences due to multiple scattering. The $\mathcal{T}$ for a cloud with the same microphysical properties over snow and ice is higher compared to over open ocean, where the majority of photons will be absorbed by the surface and are not available for new back-scattering events of the upward irradiance in the cloud towards the surface. Taking this dependence into account, the broadband $\mathcal{T}$ was used to derive the cloud optical thickness similar to the approach by Leontyeva and Stamnes (1993).

Lookup tables of $\mathcal{T}$ for a range of surface albedo between 0 and 1 and LWP between 0 and 320 $\mathrm{g\,m^{-2}}$ were simulated for the local solar zenith angle and compared to the values derived from the observations along the flight track. In the simulations, vertically homogeneous pure liquid water clouds are assumed to limit the complexity of the simulations. Therefore, in the following the LWP is referred to an equivalent LWP, because no ice water content was assumed. The cloud was located between 400 m and 600 m with a fixed r_{eff} of 8 µm, typical for Arctic clouds in this season and region (Mioche et al., 2017). These rather crude assumptions result in uncertainties of the simulated irradiance, which were quantified by Leontyeva and Stamnes (1993) as a function of surface albedo, SZA, r_{eff} and cloud optical thickness.

Similar to the simulations of $F^{\downarrow}_{\mathrm{s,cf}}$ for heterogeneous surface albedo fields, an effective albedo, which influences the local scattering processes in cloudy conditions needs to be considered in the retrieval simulations of $\mathcal{T}$ (Pirazzini and Raisanen, 2008).

The diversity of potential 3D effects induced by surface and cloud heterogeneities in the MIZ omit a specific solution for the smoothing problem of the areal averaged effective albedo and can only partially be depicted by radiative transfer modelling. To make the retrieval applicable to ACLOUD measurements and reduce the uncertainties induced by horizontal photon transport, a commonly observed cloud/surface scene, with a cloud base height of 200 m and leads with different sizes, has been simulated using 3D radiative transfer (not shown here). The estimated kernel is based on a Cauchy distribution and has a considerably smaller horizontal extent compared to the cloud-free kernel introduced in Fig. 3b, due to the the low cloud base height. Applied to the theoretical observed albedo the simulated irradiance adequately reproduces the results obtained from the 3D output, and thus, reduces for these cloud/surface scenes the uncertainties of the retrieved LWP considerably.

Nevertheless, multiple scattering, changes in cloud base height (Pirazzini and Raisanen, 2008) and 3D radiative effects due to inhomogeneous cloud/surface scenes, might induce large uncertainties in this retrieval. However, the observed I_{f} statistics indicate, that the majority of ACLOUD flights were conducted over a rather homogeneous surface, where the discussed issue is minor important. The sensitivity of the retrieval is in general higher over open water compared to over ice, since changes in $F^{\downarrow}_{\mathrm{s}}$ with increasing LWP are more pronounced.

The conversion from LWP to optical thickness (τ), as required for the parameterization by Gardner and Sharp (2010), was

https://doi.org/10.5194/acp-2019-534
Preprint. Discussion started: 23 July 2019

Atmospheric Chemistry and Physics Discussions

applied by,

$$\tau = \frac{9}{5} \cdot \frac{\mathrm{LWP}}{\varrho_{\mathrm{w}} \cdot r_{\mathrm{eff}}}, \tag{A2}$$

with the density of liquid water ϱ_{w} and the simulated r_{eff}.

Author contributions. All authors contributed to the editing of the manuscript and to the discussion of the results. JS drafted the manuscript and initialized the study. JS processed the radiation data, merged the data sets and performed the radiative transfer simulations. EJ contributed to the radiative transfer simulations and their interpretation. MW, AE and CL designed the experimental basis of this study.

Competing interests. The authors declare that they have no conflict of interest.

Acknowledgements. We gratefully acknowledge the funding by the Deutsche Forschungsgemeinschaft (DFG, German Research Foundation) – Project Number 268020496 – TRR 172, within the Transregional Collaborative Research Center "ArctiC Amplification: Climate Relevant Atmospheric and SurfaCe Processes, and Feedback Mechanisms (AC)³". The authors are grateful to AWI for providing and operating the two aircraft during the ACLOUD campaign. We thank the crews of Polar 5 and Polar 6, the technicians of the aircraft for excellent technical and logistical support. The generous funding of the flight hours for ACLOUD by AWI is greatly appreciated. Observations in Fig. 8 were made by the SHEBA Atmospheric Surface Flux Group, Ed Andreas, Chris Fairall, Peter Guest, and Ola Persson.

https://doi.org/10.5194/acp-2019-534
Preprint. Discussion started: 23 July 2019

Atmospheric Chemistry and Physics Discussions

References

Benner, T. C., Curry, J. A., and Pinto, J. O.: Radiative transfer in the summertime Arctic, J. Geophys. Res., 106, 15.173–15.183, 2001.

Cohen, J., Screen, J. A., Furtado, J. C., Barlow, M., Whittleston, D., Coumou, D., Francis, J., Dethloff, K., Entekhabi, D., Overland, J., and Jones, J.: Recent Arctic amplification and extreme mid-latitude weather, Nat. Geosci., 7, 627–637, https://doi.org/10.1038/NGEO2234, 2014.

Ehrlich, A., Stapf, J., Lüpkes, C., Mech, M., Crewell, S., and Wendisch, M.: Meteorological measurements by dropsondes released from POLAR 5 during ACLOUD 2017, PANGAEA, https://doi.org/10.1594/PANGAEA.900204, 2019a.

Ehrlich, A., Wendisch, M., Lüpkes, C., Buschmann, M., Bozem, H., Chechin, D., Clemen, H.-C., Dupuy, R., Eppers, O., Hartmann, J., Herber, A., Jäkel, E., Järvinen, E., Jourdan, O., Kästner, U., Kliesch, L.-L., Köllner, F., Mech, M., Mertes, S., Neuber, R., Ruiz-Donoso, E., Schnaiter, M., Schneider, J., Stapf, J., and Zanatta, M.: A comprehensive in situ and remote sensing data set from the Arctic CLoud Observations Using airborne measurements during polar Day (ACLOUD) campaign., Earth Syst. Sci. Data Discuss., https://doi.org/10.5194/essd-2019-96, in review, 2019b.

Emde, C., Buras-Schnell, R., Kylling, A., Mayer, B., Gasteiger, J., Hamann, U., Kylling, J., Richter, B., Pause, C., Dowling, T., and Bugliaro, L.: The libRadtran software package for radiative transfer calculations (version 2.0.1), Geosci. Model Dev., 9, 1647–1672, https://doi.org/10.5194/gmd-9-1647-2016, 2016.

Gardner, A. S. and Sharp, M. J.: A review of snow and ice albedo and the development of a new physically based broadband albedo parameterization, J. Geophys. Res., 115, F01 009, https://doi.org/10.1029/2009JF001444, 2010.

Gasteiger, J., Emde, C., Mayer, B., Buras, R., Buehler, S. A., and Lemke, O.: Representative wavelengths absorption parameterization applied to satellite channels and spectral bands, J. Quant. Spectrosc. Ra., 148, 99–115, https://doi.org/10.1016/j.jqsrt.2014.06.024, 2014.

Gillett, N. P., Stone, D. A., Stott, P. A., Nozawa, T., Karpechko, A. Y., Hegerl, G. C., Wehner, M. F., and Jones, P. D.: Attribution of polar warming to human influence, Nat. Geosci., 1, 750–754, https://doi.org/10.1038/ngeo338, 2008.

Goosse, H., Kay, J. E., Armour, K. C., Bodas-Salcedo, A., Chepfer, H., Docquier, D., Jonko, A., Kushner, P. J., Lecomte, O., Massonnet, F., Park, H. S., Pithan, F., Svensson, G., and Vancoppenolle, M.: Quantifying climate feedbacks in polar regions, Nat. Commun., 9, 1919, https://doi.org/10.1038/s41467-018-04173-0, 2018.

Grenfell, T. C. and Perovich, D. K.: Incident spectral irradiance in the Arctic Basin during the summer and fall, J. Geophys. Res., 113, D12 117, https://doi.org/10.1029/2007JD009418, 2008.

Hartmann, J., Lüpkes, C., and Chechin, D.: High resolution aircraft measurements of wind and temperature during the ACLOUD campaign in 2017, PANGAEA, https://doi.pangaea.de/10.1594/PANGAEA.900880, 2019.

Iwabuchi, H.: Efficient Monte Carlo methods for radiative transfer modeling, J. Atmos. Sci., 63, 2324–2339, 2006.

Iwabuchi, H. and Kobayashi, H.: Modeling of radiative transfer in cloudy atmospheres and plant canopies using Monte Carlo methods, Tech. Rep., 8, 199 pp., 2008.

Jäkel, E. and Ehrlich, A.: Radiance fields of clouds and the Arctic surface measured by a digital camera during ACLOUD 2017, PANGAEA, https://doi.pangaea.de/10.1594/PANGAEA.901024, 2019.

Jäkel, E., Stapf, J., Wendisch, M., Nicolaus, M., Dorn, W., and Rinke, A.: Validation of the sea ice surface albedo scheme of the regional climate model HIRHAM-NAOSIM using aircraft measurements during the ACLOUD/PASCAL campaigns, Cryosphere, 13, 1695–1708, https://doi.org/10.5194/tc-13-1695-2019, 2019.

Jeffries, M. O., Overland, J. E., and Perovich, D. K.: The Arctic shifts to a new normal, Phys. Today, 66, 35–40, 2013.

https://doi.org/10.5194/acp-2019-534
Preprint. Discussion started: 23 July 2019

Kato, S., Ackerman, T., Mather, J., and Clothiaux, E.: The k-distribution method and correlated-k approximation for a shortwave radiative transfer model, J. Quant. Spectrosc. Ra., 62, 109–121, 1999.

Knudsen, E. M., Heinold, B., Dahlke, S., Bozem, H., Crewell, S., Heygster, G., Kunkel, D., Maturilli, M., Mech, M., Rinke, A., Schmithüsen, H., Ehrlich, A., Macke, A., Lüpkes, C., and Wendisch, M.: Synoptic development during the ACLOUD/PASCAL field campaign near Svalbard in spring 2017, Atmos. Chem. Phys. Discuss., https://doi.org/10.5194/acp-2018-494, 2018.

Kreuter, A., Buras, R., Mayer, B., Webb, A., Kift, R., Bais, A., Kouremeti, N., and Blumthaler, M.: Solar irradiance in the heterogeneous albedo environment of the Arctic coast: measurements and a 3-D model study, Atmos. Chem. Phys., 14, 5989–6002, https://doi.org/10.5194/acp-14-5989-2014, 2014.

Lampert, A., Maturilli, M., Ritter, C., Hoffmann, A., Stock, M., Herber, A., Birnbaum, G., Neuber, R., Dethloff, K., Orgis, T., Stone, R., Brauner, R., Kassbohrer, J., Haas, C., Makshtas, A., Sokolov, V., and Liu, P.: The spring-time boundary layer in the central Arctic observed during PAMARCMiP 2009, Atmosphere-Basel, 3, 320–351, https://doi.org/10.3390/atmos3030320, 2012.

Leontyeva, E. and Stamnes, K.: Estimation of cloud optical thickness from ground-based measurements of incoming solar radiation in the Arctic, J. Climate, 7, 566–578, 1993.

Libois, Q., Picard, G., France, J. L., Arnaud, L., Dumont, M., Carmagnola, C. M., and King, M. D.: Influence of grain shape on light penetration in snow, Cryosphere, 7, 1803–1818, https://doi.org/10.5194/tc-7-1803-2013, 2013.

Maturilli, M.: High resolution radiosonde measurements from station Ny-Ålesund (2017-05), PANGAEA, https://doi.org/10.1594/PANGAEA.879820, 2017a.

Maturilli, M.: High resolution radiosonde measurements from station Ny-Ålesund (2017-06), PANGAEA, https://doi.org/10.1594/PANGAEA.879822, 2017b.

Mioche, G., Jourdan, O., Delanoe, J., Gourbeyre, C., Febvre, G., Dupuy, R., Monier, M., Szczap, F., Schwarzenboeck, A., and Gayet, J. F.: Vertical distribution of microphysical properties of Arctic springtime low-level mixed-phase clouds over the Greenland and Norwegian seas, Atmos. Chem. Phys., 17, 12 845–12 869, https://doi.org/10.5194/acp-17-12845-2017, 2017.

Overland, J. E., Wood, K. R., and Wang, M.: Warm Arctic–cold continents: Impacts of the newly open Arctic Sea, Polar Res., 30, 15 787, doi:10.3402/polar.v30i0.15 787, 2011.

Perovich, D. K., Grenfell, T. C., Light, B., and Hobbs, P. V.: Seasonal evolution of the albedo of multiyear Arctic sea ice, J. Geophys. Res., 107, https://doi.org/10.1029/2000JC000438, 8044, 2002.

Pirazzini, R. and Raisanen, P.: A method to account for surface albedo heterogeneity in single-column radiative transfer calculations under overcast conditions, J. Geophys. Res., 113, https://doi.org/10.1029/2008JD009815, 2008.

Pithan, F. and Mauritsen, T.: Arctic amplification dominated by temperature feedbacks in contemporary climate models, Nature, 7, 181–184, https://doi.org/10.1038/ngeo2071, 2014.

Pithan, F., Svensson, G., Caballero, R., Chechin, D., Cronin, T. W., Ekman, A. M. L., Neggers, R., Shupe, M. D., Solomon, A., Tjernstrom, M., and Wendisch, M.: Role of air-mass transformations in exchange between the Arctic and mid-latitudes, Nat. Geosci., 11, 805–812, https://doi.org/10.1038/s41561-018-0234-1, 2018.

Ramanathan, V., Cess, R, D., Harrison, E. F., Minnis, P., Barkstrom, B. R., Ahmad, E., and Hartmann, D.: Cloud-radiative forcing and climate: Results from the Earth Radiation Biudget Experiment, Science, 243, 57–63, 1989.

Randles, C. A., Kinne, S., Myhre, G., Schulz, M., Stier, P., Fischer, J., Doppler, L., Highwood, E., Ryder, C., Harris, B., Huttunen, J., Ma, Y., Pinker, R. T., Mayer, B., Neubauer, D., Hitzenberger, R., Oreopoulos, L., Lee, D., Pitari, G., Di Genova, G., Quaas, J., Rose, F. G., Kato, S., Rumbold, S. T., Vardavas, I., Hatzianastassiou, N., Matsoukas, C., Yu, H., Zhang, F., Zhang, H., and Lu, P.: Intercomparison

of shortwave radiative transfer schemes in global aerosol modeling: results from the AeroCom Radiative Transfer Experiment, Atmos. Chem. Phys., 13, 2347–2379, https://doi.org/10.5194/acp-13-2347-2013, 2013.

Ricchiazzi, P. and Gautier, C.: Investigation of the effect of surface heterogeneity and topography on the radiation environment of Palmer Station, Antarctica, with a hybrid 3-D radiative transfer model, J. Geophys. Res., 103, 6161–6178, 1998.

Schmithüsen, H.: Upper air soundings during POLARSTERN cruise PS106.1 (ARK-XXXI/1.1), PANGAEA, https://doi.org/10.1594/PANGAEA.882736, 2017.

Screens, J. A. and Simmonds, I.: The central role of diminishing sea ice in recent Arctic temperature amplification, Nature, 464, 1334–1337, 2010.

Serreze, M. C. and Barry, R. G.: Processes and impacts of Arctic amplification: A research synthesis, Global Planet. Change, 77, 85–96,doi:10.1016/j.gloplacha.2011.03.004, 2011.

Spreen, G., Kaleschke, L., and Heygster, G.: Sea ice remote sensing using AMSR-E 89-GHz channels, J. Geophys. Res., 113, C02S03, https://doi.org/10.1029/2005JC003384, 2008.

Stamnes, K., Tsay, S., Wiscombe, W., and Jayaweera, K.: A numerically stable algorithm for discrete-ordinate-method radiative transfer in multiple scattering and emitting layered media, Appl. Opt., 27, 2502–2509, 1988.

Stapf, J., Ehrlich, A., Jäkel, E., and Wendisch, M.: Aircraft measurements of broadband irradiance during the ACLOUD campaign in 2017, PANGAEA, https://doi.org/10.1594/PANGAEA.900442, 2019.

Stroeve, J. C., Serreze, M. C., Holland, M. M., Kay, J. E., Maslanik, J., and Barrett, A. P.: The Arctic's rapidly shrinking sea ice cover: A research synthesis, Climatic Change, 110, 1005–1027, doi:10.1007/s10 584–011–0101–1, 2012.

Tjernström, M., Shupe, M. D., Brooks, I. M., Persson, P. O. G., Prytherch, J., Salisbury, D. J., Sedlar, J., Achtert, P., Brooks, B. J., Johnston, P. E., Sotiropoulou, G., and Wolfe, D.: Warm-air advection, air mass transformation and fog causes rapid ice melt, Geophys. Res. Lett., 42, 5594–5602, https://doi.org/10.1002/2015GL064373, 2015.

Warren, S.: Optical Properties of Snow, Rev. Geophys. Space Phys., 20, 67–89, 1982.

Weihs, P., Lenoble, J., Blumthaler, M., Martin, T., Seckmeyer, G., Philipona, R., de la Casiniere, A., Sergent, C., Gröbner, J., Cabot, T., Masserot, D., Pichler, T., Pougatch, E., Rengarajan, G., Schmucki, D., and Simic, S.: Modeling the effect of an inhomogeneous surface albedo on incident UV radiation in mountaineous terrain: determination of an effective surface albedo, Geophys. Res. Lett., 28, 3111–3114, 2001.

Wendisch, M., Pilewskie, P., Jäkel, E., Schmidt, S., Pommier, J., Howard, S., Jonsson, H. H., Guan, H., Schröder, M., and Mayer, B.: Airborne measurements of areal spectral surface albedo over different sea and land surfaces, J. Geophys. Res., 109, Art. No. D08 203, https://doi.org/doi:10.1029/2003JD004392, 2004.

Wendisch, M., Brückner, M., Burrows, J. P., Crewell, S., Dethloff, K., Ebell, K., Lüpkes, C., Macke, A., Notholt, J., Quaas, J., Rinke, A., and Tegen, I.: Understanding causes and effects of rapid warming in the Arctic, Eos, 98, https://doi.org/10.1029/2017EO064803, 2017.

Wendisch, M., Macke, A., Ehrlich, A., Lüpkes, C., Mech, M., Chechin, D., Barrientos, C., Bozem, H., Brückner, M., Clemen, H.-C., Crewell, S., Donth, T., Dupuy, R., Ebell, K., Egerer, U., Engelmann, R., Engler, C., Eppers, O., Gehrmann, M., Gong, X., Gottschalk, M., Gourbeyre, C., Griesche, H., Hartmann, J., Hartmann, M., Herber, A., Herrmann, H., Heygster, G., Hoor, P., Jafariserajehlou, S., Jäkel, E., Järvinen, E., Jourdan, O., Kästner, U., Kecorius, S., Knudsen, E. M., Köllner, F., Kretzschmar, J., Lelli, L., Leroy, D., Maturilli, M., Mei, L., Mertes, S., Mioche, G., Neuber, R., Nicolaus, M., Nomokonova, T., Notholt, J., Palm, M., van Pinxteren, M., Quaas, J., Richter, P., Ruiz-Donoso, E., Schäfer, M., Schmieder, K., Schnaiter, M., Schneider, J., Schwarzenböck, A., Seifert, P., Shupe, M. D., Siebert, H., Spreen, G., Stapf, J., Stratmann, F., Vogl, T., Welti, A., Wex, H., Wiedensohler, A., Zanatta, M., and Zeppenfeld, S.: The Arctic cloud

https://doi.org/10.5194/acp-2019-534
Preprint. Discussion started: 23 July 2019

Atmospheric Chemistry and Physics Discussions

puzzle: using ACLOUD/PASCAL multi-platform observations to unravel the role of clouds and aerosol particles in Arctic amplification, B. Am. Meteorol. Soc., 100 (5), 841–871, https://doi.org/10.1175/BAMS-D-18-0072.1, 2019.